PEER REVIEWED

# Microstructural, Mechanical and Wear Properties of Atmospheric Plasma-Sprayed and High-Velocity Oxy-Fuel AlCoCrFeNi Equiatomic High-Entropy Alloys (HEAs) Coatings

A. Silvello[1] · E. Torres Diaz[1,2] · E. Rúa Ramirez[1,2] · I. Garcia Cano[1]

**Abstract** In this investigation, atmospheric plasma spray (APS) and high-velocity oxy-fuel (HVOF) techniques were used to produce AlCoCrFeNi coatings. High-entropy alloys (HEAs), due to their mechanical, chemical, and physical properties are capturing the attention of the international scientific community. Starting feedstock powders were characterized in terms of size, phase, and size, and corrosion test in NaCl, ball on disk, rubber wheel, and jet erosion tests was carried out on the obtained coatings. The results of the tribological investigation show that in the case of APS coatings, corrosion and wear behavior depend on the microstructure phases of the coating, as well as the amount of oxides. In particular, the wear morphology of APS surfaces is characterized by brittle fracture, with the presence of pores, cracks, and grooves. For HVOF coatings, further investigations on process parameters are

needed because of the poor adhesion strength between the coating and the substrate. Anyway, the obtained corrosion resistance of HVOF coating is greater than that of the C steel substrate used to benchmark the results, and in addition, it ensures better performances in rubber wheel and jet erosion tests, but its wear resistance in the ball-on-disk test is worse because of the debris remaining in the wear track.

✉ A. Silvello
asilvello@cptub.eu

1    Thermal Spray Centre (CPT), University of Barcelona, Martí i Franqués 1, 08028 Barcelona, Spain

2    Engineering Research and Development Group in New Technologies (GIDINT), Santo Tomás University, Tunja, Colombia

## Introduction

Yeh et al. (Ref 1) and Cantor et al. (Ref 2) have defined equiatomic HEAs as a new type of material distinguished by multiple principal elements in the same quantity, at least four or five. Their excellent mechanical and tribological properties, such as hardness, ductility, and corrosion resistance, are due to four different peculiarities: the high-entropy effect, the lattice torsion, the delayed diffusion effect, and the cocktail effect (Ref 3, 4). Obviously, the international scientific community was attracted to the mechanical properties of this new class of materials because of their potential industrial application, but the cost of raw materials is still a limit (Ref 5). It is no doubt that the most investigated equiatomic HEAs are FeCoCr-NiMn (Cantor Alloy) and AlCoCrFeNi alloys (Ref 6, 7, 8, 9), but the new trend is to study new classifications as well as new compositions. It is very interesting to remark on the work of Pan et al. (Ref 10) in which it was carried out a review of HEMs (high-entropy materials), such as HEOs (high-entropy oxides) or HECs (high-entropy ceramics) for catalysis applications. To continue this

general introduction about HEAs and their new potential composition, it is worth remembering the "refractory" HEAs. Fan et al. (Ref 11) have demonstrated a combination of high strength, good tensile ductility, high fracture toughness, and excellent high-temperature properties of HfNbTaTiZr alloy for aerospace applications, while Zeng et al. (Ref 12) have shown that the impact toughness of $Ti_3Zr_{1.5}NbVAl_{0.25}$ alloy has better performance than most traditional HEAs. To conclude this brief overview of different HEAs, Fu et al. (Ref 13) have collected and resumed their potential applications in the energy sector, looking for the correlation between their microstructure (FCC, BCC and so on) and their mechanical performances.

Atmospheric plasma spray and high-velocity oxy-fuel are well-known and well-established thermal spray processes utilized in different industrial sectors, and of course, nowadays they are investigated to deposit HEAs coatings on metallic substrates. For example, Meghwal et al. (Ref 14) have studied the electrochemical performances of plasma-sprayed AlCoCrFeNi coatings in seawater, and results have shown that the behavior of HEAs coatings was similar to that of 316L stainless steel. Zhang et al. (Ref 15) have studied the passivation mechanism of the same plasma-sprayed alloy onto AISI 1045 steel, demonstrating that the increase in Al content in AlCoCrFeNi coating enhances its oxidation resistance. Other investigations (Ref 16, 17) have shown that adding to AlCoCrFeNi alloy elements with larger atomic radius (such as Ti) improves the hardness and wear resistance of the coating. For this reason, Tian et al. (Ref 18) have demonstrated that the wear resistance of AlCoCrFeNiTi coating performed better than the laser cladding NiCrBSi coating. Not only APS, but also HVOF was utilized to produce HEAs coatings. Meghwal et al. (Ref 19) have demonstrated that AlCoCrFeNi coating produced via HVOF has a good corrosion resistance compared with 316L stainless steel, but also the coating has shown pitting corrosion phenomena. Löbel et al. (Ref 20) have concluded that AlCoCrFeNi coatings deposited via HVAF (high-velocity air fuel) showed better corrosion resistance than those produced via HVOF, probably due to the denser passive layer. Moreover, Preuß et al. (Ref 21) have investigated EHEAs (eutectic high-entropy alloys) such as $Al_{0.3}CoCrFeNiNb_{0.5}$ and $Al_{0.3}CoCrFeNiMo_{0.7}$ deposited using the HVOF process. Their results have shown that metastable phases positively influenced the wear performances of the HVOF coatings.

In this fast-moving scenario, the aim of the present paper is to investigate the mechanical and tribological properties of AlCoCrFeNi coatings deposited via APS and HVOF and to compare the obtained results with those available in the literature. The APS and HVOF process parameters were optimized focusing on the thickness and porosity level of the coatings, and the results of the wear and corrosion tests were carried out, which could be useful in determining whether the coatings can be used in harsh environments.

## Materials and Methods

HEAs starting powders characterization, coatings deposition, as well as characterization and testing, were carried out at the facilities of the Thermal Spray Centre (CPT) at the University of Barcelona (Barcelona, ES). The coatings were deposited on a low C steel substrate. These low C steel substrates and 316L bulks, as well as the setup of all equipment for each test (adhesion strength, hardness, corrosion resistance, rubber wheel, ball on disk, jet erosion test), are the same as our previous work (Ref 22). To obtain benchmark values, the performances of the deposited coatings were compared to the bulks mentioned before.

### Powders Characterization

Equiatomic HEAs powders (AlCoCrFeNi, Greenheart Industry Co. LTD, CN) were characterized by shape, chemical composition, XRD phase analysis, particle size distribution, apparent density, and flow rate.

For particle size distribution determination, the laser scattering (LS) technique was used in a Beckman Coulter LS 13 320 (Brea, CA, USA) equipment, in accordance with the ASTM B822-02 on dry via mode. Scanning electron microscopy (SEM, Thermo Fisher Phenom Pro Desktop, Eindhoven, NL) was used for image obtention. The technique x-ray diffractometry (XRD) in an equipment Malvern PANalytical X'Pert PRO MPD $\theta/\theta$ Bragg–Brentano with X'Pert software (Malvern, United Kingdom) was used for phase analysis, with font of Co K$\alpha$ ($\lambda$ = 1.7903 Å) and work power 45 kV-40 mA. The apparent density of the powders was measured, in accordance with the ASTM B-212-99, as the flow rate, in accordance with the ASTM B-213-03 (Table 1).

### Coatings Deposition

Plasma-Technik AG A300 gun (CH) was used to produce plasma-sprayed coatings, while Oerlikon (Sulzer) Metco (Pfäffikon, CH) Diamond Jet Hybrid DJH 2600 equipment

**Table 1** Chemical composition (atomic %) of AlCoCrFeNi alloy

|            | Al    | Co    | Cr    | Fe    | Ni    |
| ---------- | ----- | ----- | ----- | ----- | ----- |
| AlCoCrFeNi | 21.23 | 20.17 | 19.29 | 19.47 | 19.83 |

was employed for HVOF coatings. Substrates were grit-blasted with alumina (F24) before the deposition process up to roughness Ra $\approx$ 7. The process parameters used for APS and HVOF deposition are presented in Tables 2 and 3.

## Coatings Characterization

Metallographic cross-section preparation was executed in accordance with the ASTM E1920-03. SEM (JEOL JSM 6510, JP) was used to observe the microstructure of the coatings. Using the ImageJ software and according to the test method B of ASTM E2109-14, the porosity was calculated by grayscale threshold in OM (Leica DMI 5000) images of the microstructure. For each coating, seven porosity measurements were analyzed. The Shimadzu HMV (Tokyo, JP) was used for 10 measures of micro-hardness in the Vickers scale for each coating, with a load of 0.3 kgf ($HV_{0.3}$).

## Corrosion Test

In compliance with the ASTM G59-97 and ASTM G102-89, potentiodynamic polarization measurements were carried out to determine the corrosion current density, polarization resistance, and corrosion rate of the coatings. A 3.5 wt.% NaCl water solution at room temperature was used. For each coating and reference bulk, two different samples were used for corrosion tests as working electrode, with an exposed area of 1.0 $cm^2$. The exposed surfaces were grinding up to 1200 mesh and maximum roughness of Ra 0.3 μm. A saturated calomel (3.0 M KCl) was the reference electrode, and platinum was the counter electrode in the tests. A scan rate of 0.05 mV $s^{-1}$ and a potential range from Ecorr $\pm$ 25 mV were used to acquire the polarization resistance, and Ecorr from $-$ 250 to 1050 mV was used to acquire the anodic and cathodic Tafel slopes.

## Adhesion Test

The adherence of the coatings was carried out in compliance with ASTM C633-13. The adhesive agent used was the HTK Ultra Bond 100 (Hamburg, D), with measured adherence of 73.7 $\pm$ 1.2 MPa (four measures were done). The equipment used was the Servosis MCH-102 ME

(Madrid, ES). The results of the adherence were classified interpreting as adhesive, cohesive, and bonding failure.

## Sliding Wear Test (Ball on disk)

The test was executed in accordance with the ASTM G99-04, using a CM4 Enginierya S.L. (Barcelona, Es) equipment. Ball-on-disk testing consists of the friction between a disk and a ball, without lubrication conditions. The vertical force applied to the WC–Co ball was 10 N, and the surface of the samples tested was previously prepared by grinding and polishing until the maximum roughness Ra 0.8 μm. The tests were performed at room temperature (27 $\pm$ 2 °C) and maximum 20% moisture without any lubricant. The coefficient of friction (CoF) between the WC–Co ball and the HEAs coating was measured and this value was plotted.

## Abrasive Wear Test (Rubber wheel)

In accordance with the ASTM G65-00, the low-stress abrasion test (Rubber wheel) consists of erosion wear with a third body, where a rubber wheel rotates against the surface of the sample. This contact is done with a determined load, and a constant feed of abrasive material between the wheel and the sample shows how this abrasive test works and the equipment (CM4 Enginierya S.L., Barcelona, ES). $SiO_2$ abrasive particles produced by Sibelco (Barcelona, ES) were fed in dry conditions (less than 0.5% moisture). The mass of the sample was measured in different elapsed times of testing, using an equipment Mettler AE100 (Columbus, OH, USA).

## Jet Erosion Test

In the jet erosion test (ASTM G73-10), a sample is abraded by repeated impacts of water jets until the degradation/destruction of the coating. The jet erosion apparatus (Fig. 5a, CM4 Enginierya S.L., Barcelona, ES) in CPT facilities consists of two water jets and a central rotating arm that can reach high rotation speed. At the end of the arm, a sample holder keeps the sample parallel to the water jets. The water jet diameter is 4 mm, and the process parameters are water pressure (variable from 0.1 to 2.0 Bar), rotation speed (variable from 50 up to 350 km/h), and test time. The experiments were carried out at 190 km/h,

**Table 2** Parameters used for APS process

| Current and voltage | Ar, l/m | H₂, l/m | Carrier gas, l/m | Standoff distance, mm | Robot speed, mm/s | Stir, rpm | Step, mm | Layers |
|---|---|---|---|---|---|---|---|---|
| 600 A, 65 V | 35 | 12 | 1.5 | 130 | 500 | 30 | 5 | 46 |

**Table 3** Parameters used for HVOF process

| H$_2$ flow mass rate | O$_2$ flow mass rate | Comp. air flow mass rate | Powder feed, g/m | Standoff distance, mm | Robot speed, mm/s | Step, mm | Layers |
|---|---|---|---|---|---|---|---|
| 80 | 37 | 7 | 30 | 275 | 250 | 5 | 40 |
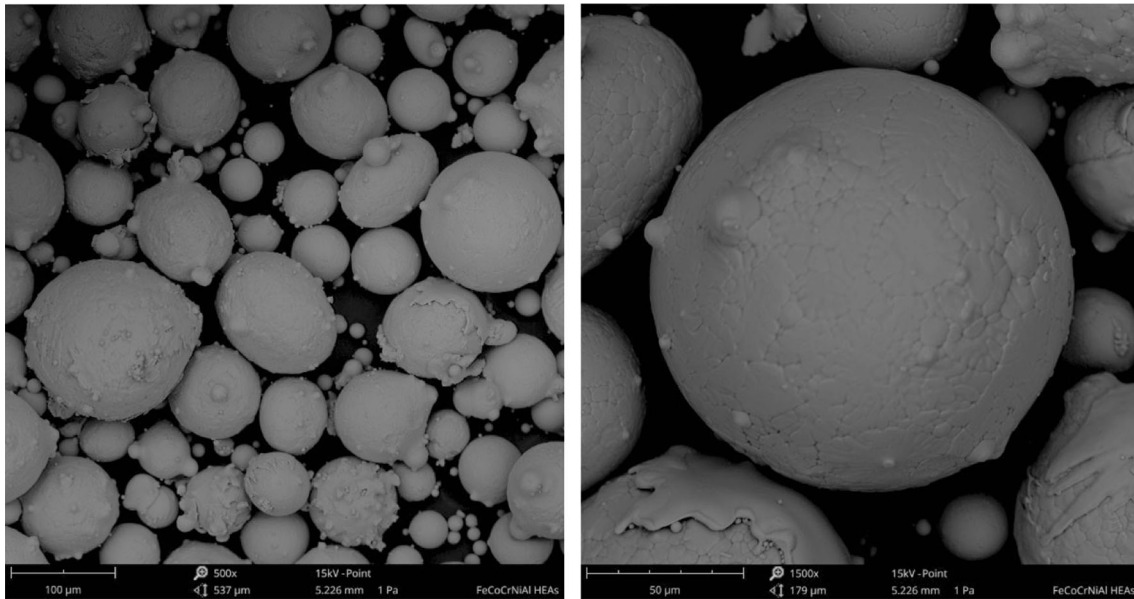


**Fig. 1** (a) SEM image of starting feedstock powders and (b) high magnification

with the pressure of water set up at 1 Bar, controlling every 30 min the sample to measure the weight loss and the damaged area. The test was repeated 3 times for each sample.

## Result and Discussion

### Powders Properties

As shown in Fig. 1(a) and (b), gas atomized starting feedstock powders have a dendritic regular shape (quasi-spherical), with a mean particle size of 82.55 μm (Fig. 2). According to Ref 23, the presence of satellites is due to the interaction between larger particles and finer ones during the gas atomization process. Because of their smaller size, finer particle powders hit the bigger ones with high velocity and solidify more rapidly than those. This phenomenon is more evident in the case of a marked size difference between the particle and its satellite, as in the case of our starting feedstock powders. The XRD analysis in Fig. 3 confirmed that starting microstructure of the powders is mainly BCC (Ref 19, 20, 24, 25), with the presence of A2 and B2 phases. The apparent density and the flow rate

values are similar to the FeCoCrMnNi Cantor alloy of our previous work (Ref 22).

### Coatings Characterization

Considering our previous experiences (Ref 26, 27, 28, 29), APS and HVOF process parameters such as the flow rate of carrier gas, standoff distance between gun and substrate, robot arm velocity, and oxygen flow mass rate were chosen in order to obtain dense and thick coatings.

#### Plasma Coatings

*Microstructure* Figure 4 shows the microstructure of obtained plasma-sprayed coating. Some coarse pores are visible, even if the microstructure is dense, homogeneous, and with a thickness of about 430 μm without spallation and cracks, due to the choice of the process parameters mentioned above. XRD analysis in Fig. 3 reports the same peaks of starting feedstock powders, but is well-visible an enlargement and a broadening. The broadening of the peaks means that grain refinement occurred (Ref 30), and it is well-known that the rise of diffraction peaks intensity is expected during the plasma spray process, as a result of a

**Fig. 2** Laser scattering of starting feedstock powders
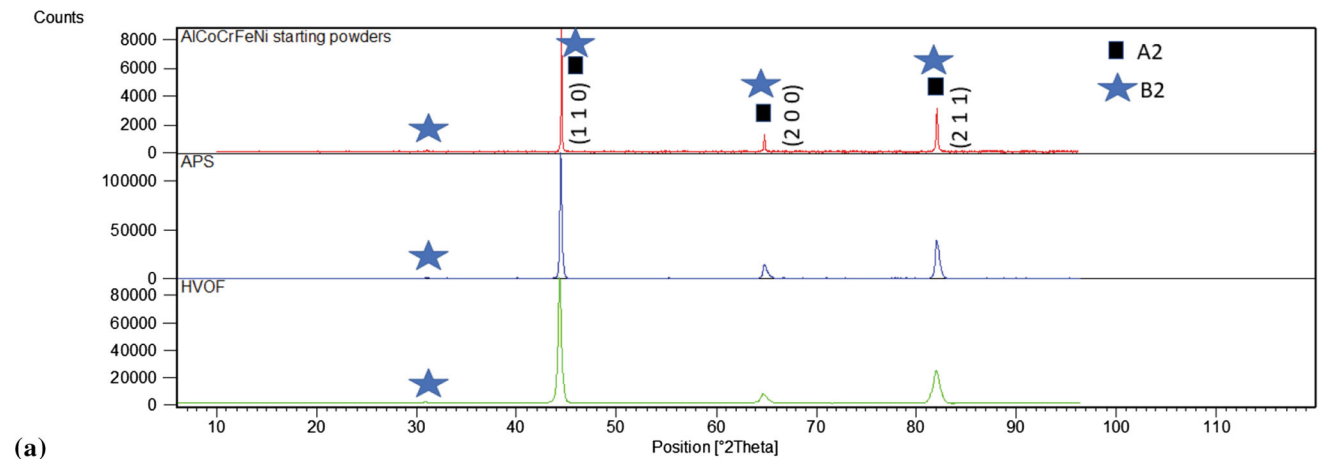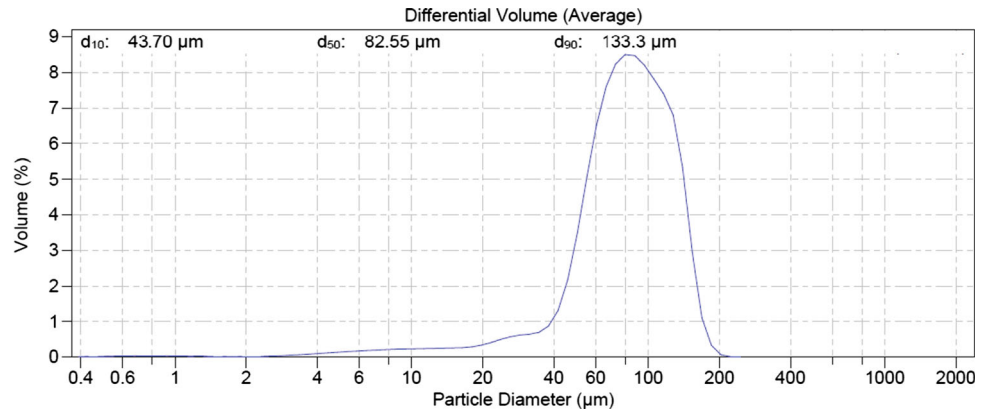




**(a)**
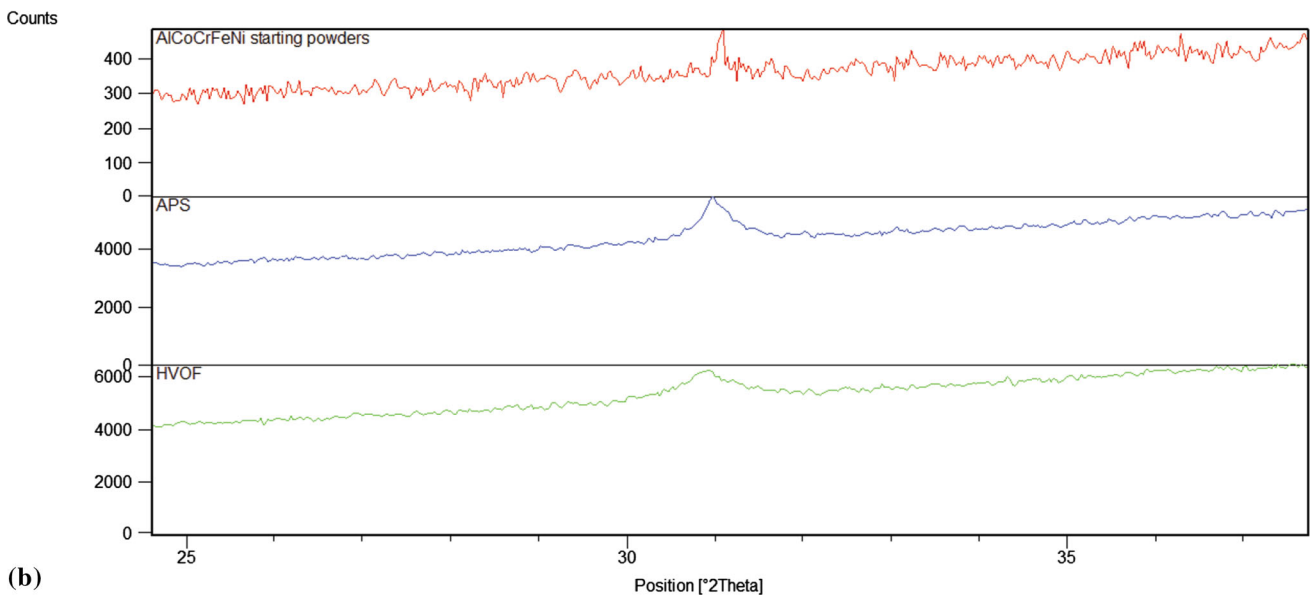


**(b)**

**Fig. 3** (a) XRD analysis, (b) XRD analysis, high magnification of B2 31° peak

modification of the lattice parameters (Ref 31). The SEM image in Fig. 5 reveals the presence of two main different phases, a dark gray phase (marked as "A") richer in Al than the light gray phase (marked as "B"). EDS analysis in Fig. 6(a) and (b) shows that Fe, Co, and Ni are uniformly present in the coating, with a low level of oxygen, and the
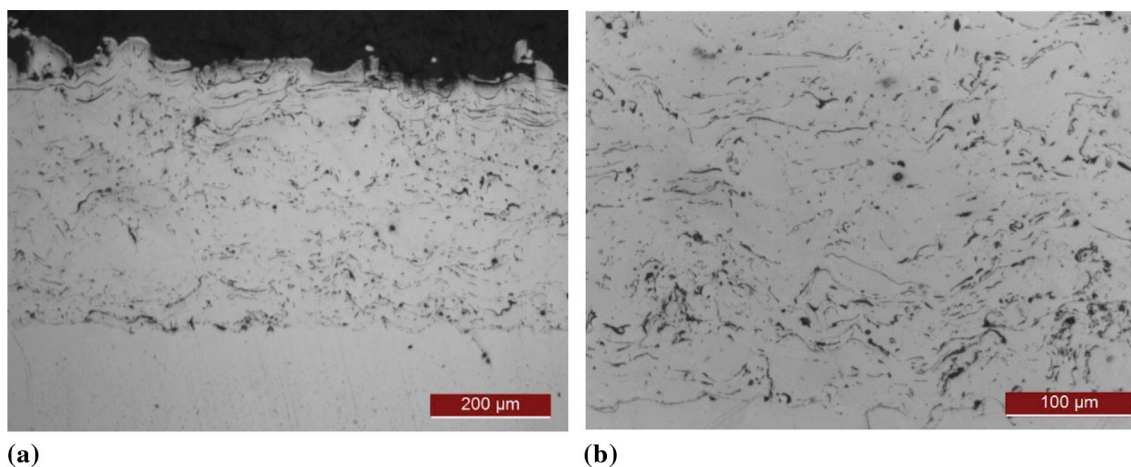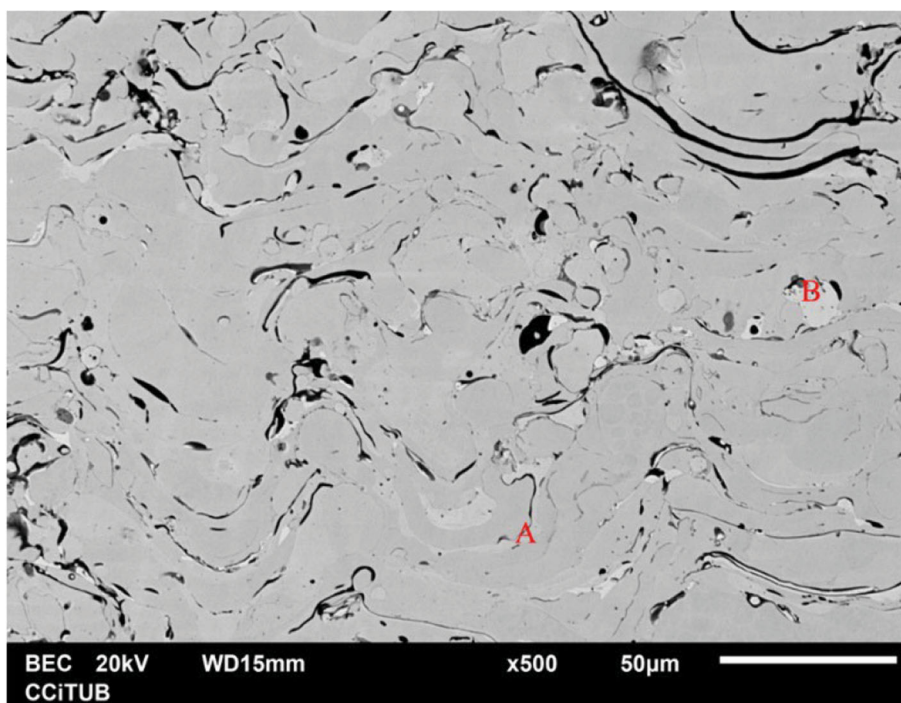
**Fig. 4** (a) OM APS coating, (b) high magnification

**Fig. 5** SEM APS coating



more visible oxide (black phase in Fig. 6a) is probably Al2O3. These results are in line with Ref 32, and probably due to the very low amount, XRD analysis did not detect FCC compounds.

*Adhesion Strength and Hardness* Low oxides content, according to (Ref 33), could affect positively the adhesion strength between the sprayed particles, and in fact, the measured adhesion strength of our plasma-sprayed coatings was 61 ± 3 MPa. The failure mechanism was cohesive, and analyzing the fracture morphology of the plasma-sprayed coating in Fig. 7(a) and (b), it can be observed that there are no dimples, while the red arrows indicate the presence of few short striations. The failure took place in the inner contact zone between the lamellar structure of the molten particles, probably due to the presence of microcracks and few oxides, leaving a smooth surface. This failure mode is confirmed for thermal spray technologies in Ref 34, 35. The local short striations represent the zone of crack initiation and propagation (Ref 36). They look like small steps and can be classified as classical ductile striations (Ref 37); even if as expected from the BCC phase, brittle fracture is the main mechanism (Ref 38). The hardness value of the APS coating is 367 ± 22 $HV_{0.3}$ and confirms the results of a previous investigation (Ref 39), in which it was underlined that the hardness of an
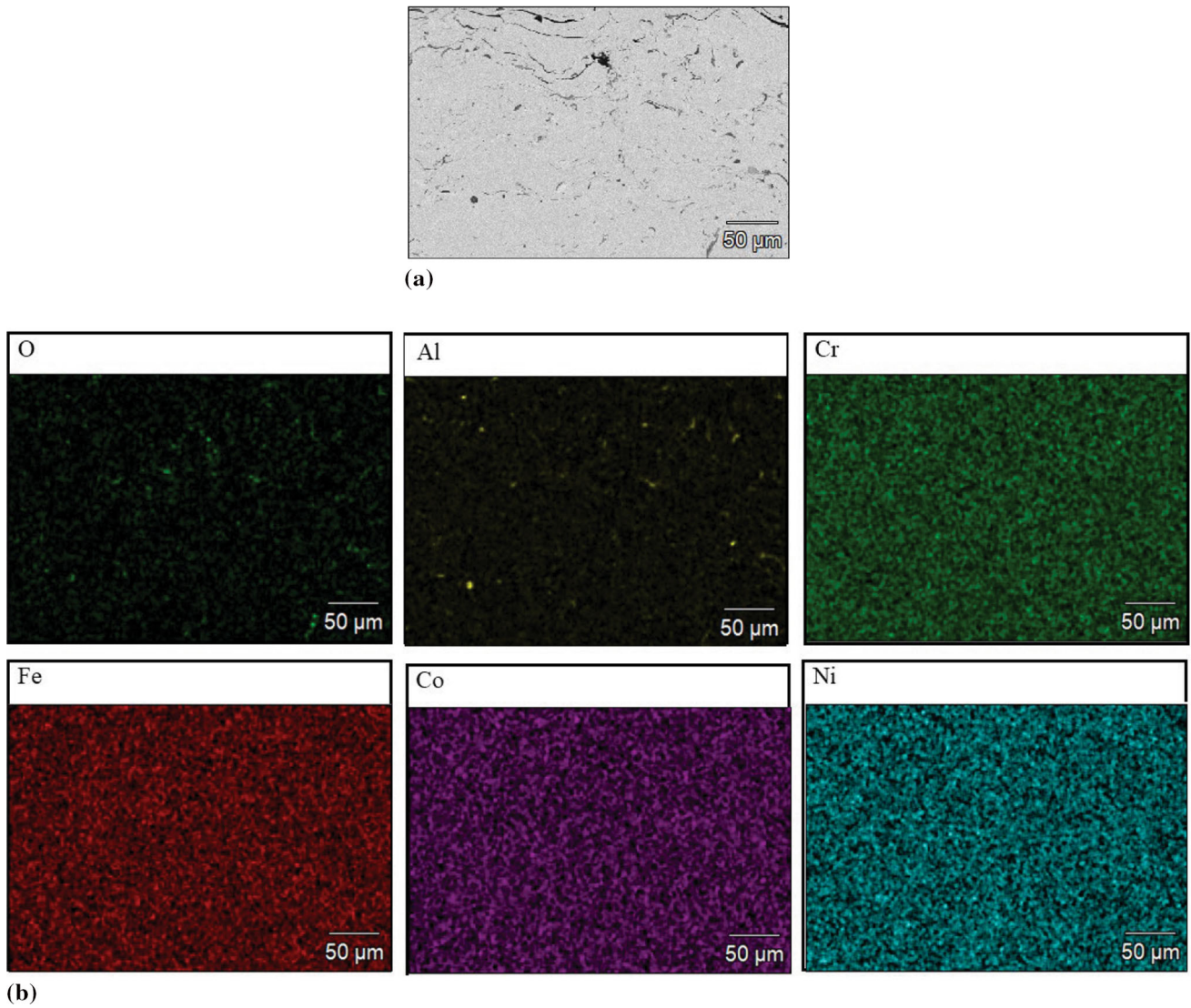
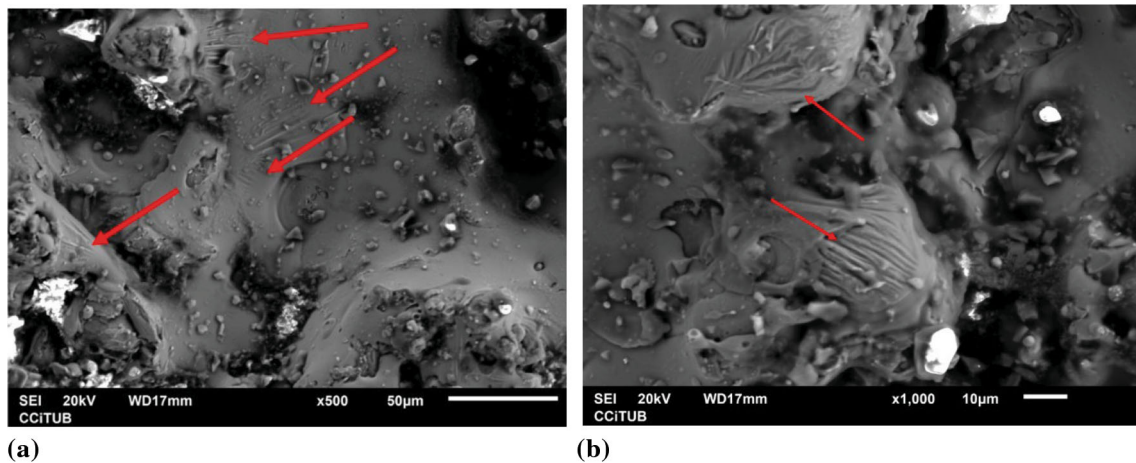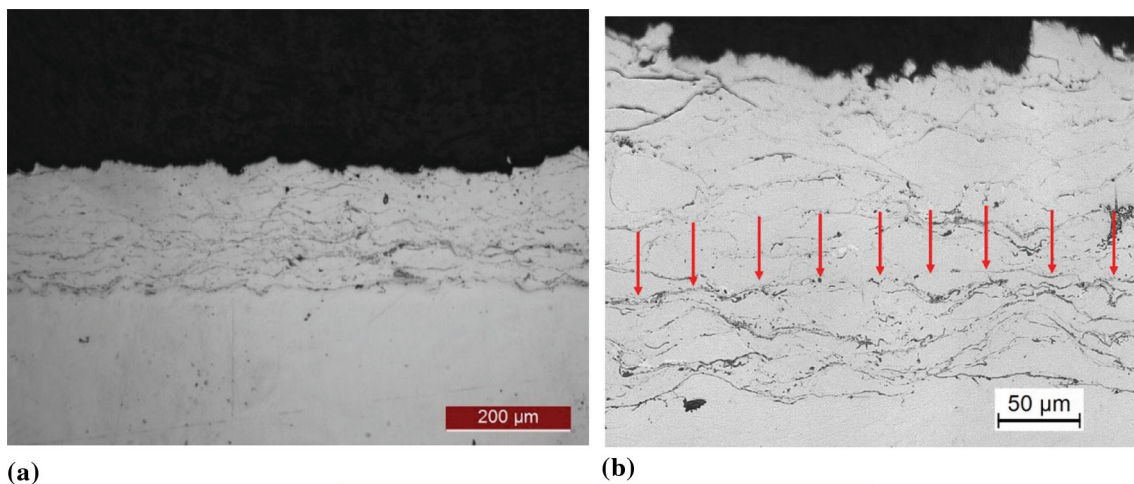Fig. 6 (a) APS coating, (b) EDS analysis of APS coating in Fig. 6a



Fig. 7 (a) SEM fracture surface of plasma-sprayed coating, (b) high magnification of local striations

**Table 4** Starting feedstock powders characterization

| Particle size distribution, μm | Apparent density, g cm$^{-3}$ | Flow rate, g s$^{-1}$ |
|---|---|---|
| Mean 82.55 | 4.00 ± 0.03 | 3.30 ± 0.21 |



**Fig. 8** (a) OM HVOF coating, (b) high magnification

**Table 5** Coatings characterization

| | Thickness, μm | Hardness, HV$_{0.3}$ | Porosity, % | Adhesion strength, MPa |
|---|---|---|---|---|
| APS | 430 ± 24 | 367 ± 22 | 5 | 61 ± 3 |
| HVOF | 186 ± 10 | 502 ± 46 | 2 | 15 ± 1 |

AlCoCrFeNi plasma-sprayed coating depends on the size of starting feedstock powders, that is, the larger the mean size, the greater the hardness (Table 4).

*HVOF Coatings*

*Microstructure* Figure 8 shows the OM microstructure of the HVOF coating. In this case, we can observe a dense and uniform coating with a thickness of around 186 μm, also a few pores, and low oxides content, but some decohesion zone between the particles. As reported in Table 5, the APS coating thickness (430 ± 24 μm) is twice that of HVOF one, even if the number of deposited layers is almost the same. Looking at Tables 2 and 3, it is possible to see that in the case of the APS process, the standoff distance between the gun and substrate is approximately half in comparison with HVOF one, while the speed of the robot arm is twice as fast. The higher temperature of the APS process, the shorter distance between the substrate and the gun, and the higher robot arm speed reduce the time interval between the impacts of subsequent particles. For this reason, in the case of the APS process in comparison with HVOF, the next particle crashes onto a hotter previous splatted particle. The higher temperature of previously deposited particle well-affects the deformability of the BCC feedstock powders, resulting in a higher deposition efficiency and in higher adhesion strength. Similar results were reached by Valarezo et al. (Ref 40) that studied APS and HVOF processes defining the interval splat time, or in Ref 41 using different starting feedstock materials. In addition, the APS process parameters used affect not only the deposition efficiency, but also the amount of oxides in the coating. It is well-known that in general terms, the in-flight speed of APS particles is lower than that of HVOF ones, and this is the reason why APS particles spent more time in-flight, and consequently, they are characterized by relatively higher oxidation (Ref 42, 43, 44). In the case of our APS deposition process, the standoff distance between the gun and the substrate and the robot speed both contribute to a lower time in-flight of the particles, and for this reason, the oxidation level of both APS and HVOF coatings is low and similar.

The HVOF coating retains the same peaks (Fig. 3) of starting feedstock powders. Also, it is well-visible a broadening of the peaks, even if the enlargement is less than that observed in the case of APS coating. This broadening of the peaks in the HVOF and APS deposition processes is well-known as a consequence of the residual

**Fig. 9** SEM HVOF coating
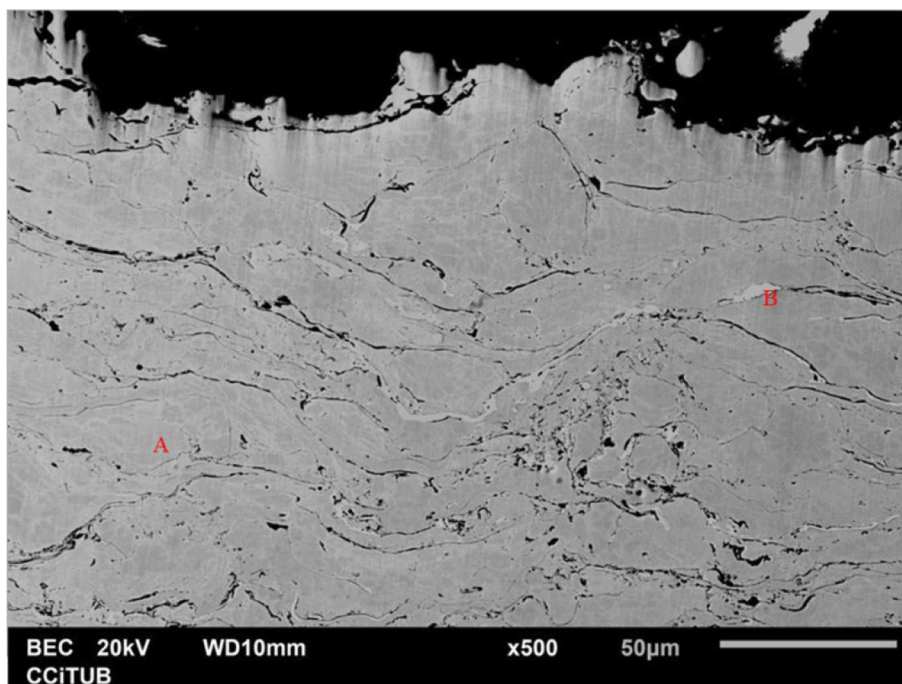


stresses generated by the particle deformation and cooling, as well as the grain refinement, that change the lattice parameters (Ref 45). In the present study, starting feedstock powders and both thermally sprayed coatings show only order and disorder BCC phases, in contrast with other investigations in which is present FCC phase too. This difference is probably due to the gas atomization process of the commercial starting feedstock powders because different process parameters can lead to the no formation of additional phases (Ref 39, 46). In any case, the SEM image in Fig. 9 shows two main phases, phase "A" is richer in Al and phase "B" poorer. As in the case of APS coating, Fe, Co, Cr, and Ni are uniformly distributed (Fig. 10a and b), while are well-visible fewer overlapping areas between Al and oxygen, and consequently, the coating presents less amount of Al2O3 oxide and XRD did not detect FCC phases.

*Adhesion Strength and Hardness*   In comparison with the adhesion strength of APS coating (61 MPa), the HVOF value is very low, around 15 MPa. Probably, it depends on the region of decohesion between deposited particles, as well as the deposition parameters process because in Fig. 11(a), the red arrow indicates a well-visible non-melted particle. In Fig. 8(b), the arrows indicate a thin and continuing black line between two deposition layers, and it is possible to see something similar along all the closer layers to the substrate. This "trans-layers" black line, being probably an oxidation region, acts as a crack propagation line. In addition, this black line shows a very flat impact

surface, denoting probably a low-impact velocity of the particles due to the large distance from the substrate (275 mm), resulting in no optimal particle deformation. This flat impact surface seems to be less visible far from the substrate, confirming that the choice of the SOD may not have been the best. The HVOF process parameters used in this investigation were chosen looking for the greatest thickness of the coating, but microstructure images and adhesion strength value suggest further investigations. Figure 11(b) shows the fracture surface morphology of the HVOF coating and well-visible dimples that indicate a localized ductile fracture mechanism. The hardness value of the HVOF coating is $502 \pm 46$ $HV_{0.3}$, higher than APS coating ($367 \pm 22$ $HV_{0.3}$). Even if both coatings are characterized by the same BCC structure, the higher value of HVOF coating is due to its lower porosity, although this hardness makes the coating brittle. These results are similar to those in Ref 19 and according to Ref 47, the limitation of dislocation movement is explained. Moreover, in the case of the HVOF process, it is well-known that higher hardness values are expected due to the inherent characteristics of the process itself (Ref 48), as well as has been demonstrated by an inverse relationship between porosity and hardness (Ref 49).

## Corrosion Properties

Figure 12 shows not only the polarization curves of the APS and HVOF coatings, but also those of 316L and C steel substrates used to perform the benchmark. Both
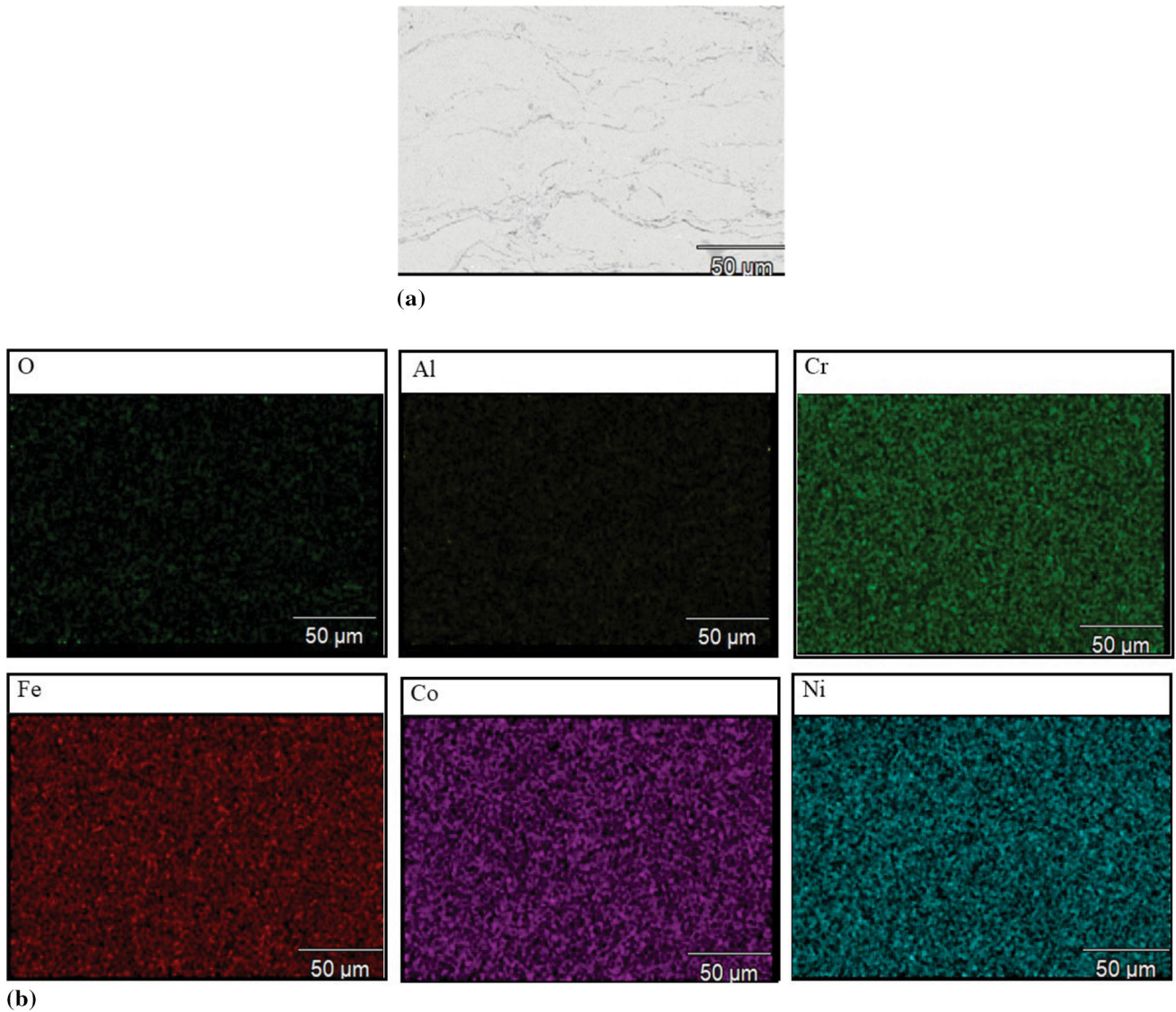
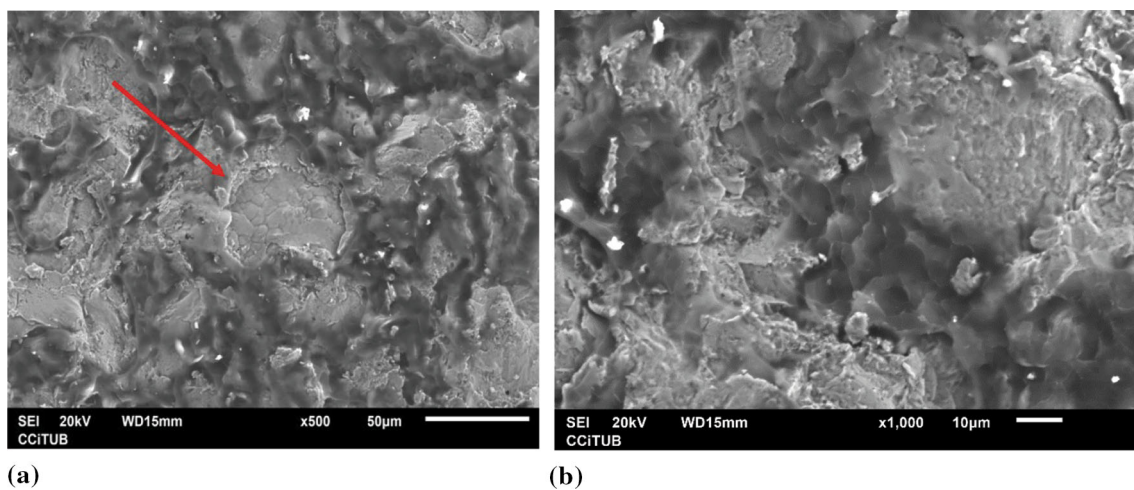**Fig. 10** (a) HVOF coating, (b) EDS analysis of HVOF coating in Fig. 10a



**Fig. 11** (a) SEM fracture surface of HVOF coating, (b) high magnification of fracture surface of HVOF coating, dimples
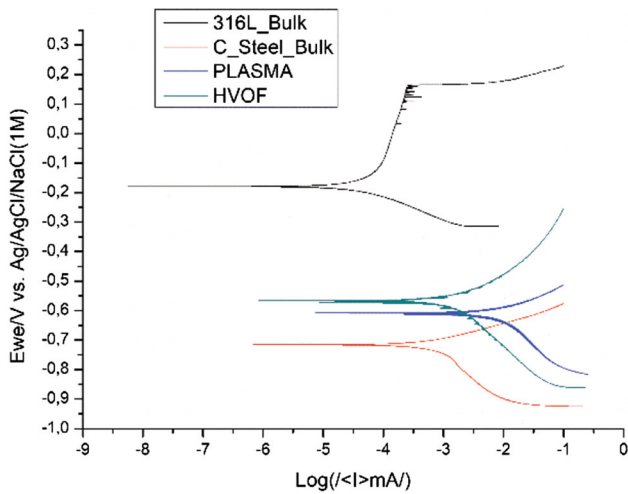
**Fig. 12** Polarization curves

**Table 6** $E_{corr}$ and $I_{corr}$ values

|  | $E_{corr}$, mV | $I_{corr}$, µA |
| --- | --- | --- |
| APS | − 608 | 0.70 |
| HVOF | − 587 | 0.53 |
| 316L bulk | − 195 | 0.04 |
| C steel bulk | − 730 | 0.50 |

coatings preserved the C steel substrate enhancing its performance, but in comparison with our previous investigation in which we deposited Cantor alloy via HVOF and cold spray (Ref 22), the results are slightly worse. In particular, the results reached in our previous study spraying Cantor alloy via HVOF were due to the increased amount of Co oxides and Fe oxides in comparison with that of this investigation. To confirm this, Ref 14 shows how the presence of different oxides contributed to corrosion resistance. Even if both coatings of the present investigation protect the C steel substrate also thanks to their very low porosity, their performances are far from 316L bulk, while in our previous investigation, the behavior of HVOF Cantor alloy coating was close to stainless steel. Despite Al and the higher Cr and Ni content percentage in comparison with the 316L bulk, both APS and HVOF AlCoCrFeNi coatings did not reach similar performance. The potential and current corrosion values of both coatings and both substrates used to carry out the benchmark are listed in Table 6.

### Sliding Wear Test

For both coatings, the coefficient of friction (CoF) was calculated when the system achieved a stationary behavior, after 15.000 cycles. As visible in Fig. 13(a), for APS coating, the wear track width is $950 \pm 14$ µm, and the main wear mechanism is adhesive type because there are no furrows and debris because they were rolled and adhered on the wear track, leaving a smooth and plastically deformed surface, with splat delamination (red box in Fig. 13b).

A similar wear surface morphology is visible in Ref 50, 14. In general terms, it is well-known that the lamellar microstructure of APS coating has its weak point in inter-

splat bonding (Ref 51), inducing a high-volume loss through the delamination of the deposited particles. Also, there is no ordered orientation of the microcracks, and this aspect suggests a brittle failure mechanism, due to the BCC microstructure of the coating. Due to the brittle behavior, the coating broke in the shape of fine debris that are pulled out during the rapid crack growth, and subsequently, they were rolled on the wear track. This mechanism was proposed in Ref 14 for APS coatings containing brittle oxides with different hardness. For what has been said previously, the morphology of the wear track of Cantor alloy deposited in our previous work (Ref 22) is completely different in comparison with the wear track of APS AlCoCrFeNi coating, due to the presence of the more ductile FCC phase.

For HVOF coating, the wear track width is $1213 \pm 21$ µm, and Fig. 14(b) shows visible typical cracks of a brittle fracture. The wear mechanism is abrasive, due to the presence of wear grooves (Ref 52) in the wear track, as visible in Fig. 14(c) looking at the red arrows. As reported in Table 7, this wear mechanism and the higher hardness of the HVOF coating result in a higher volume loss in comparison with APS coating. The hard debris acted as a third body between the WC–Co ball and the coating, worsening its performance, while in the case of APS coating, the debris were rolled on the surface (Fig. 15).

### Rubber Wheel Test

The abrasive wear rates of both 316L and C steel bulks and APS coating are listed in Table 8. The duration of the test was set at 30 min and the trend of abrasive wear rate of APS coating and C steel bulk seems the same (Fig. 17) because, after 540 s, the APS coating was completely abraded up to the substrate. To better understand why the coating was totally worn down, Fig. 16 shows the damaged coating zone close to the region where the coating was completely erased, and it is possible to see some grooves, cracks, and a lot of pores.

According to BCC phases present in the coating, the wear morphology suggests a brittle damage mode, and pores depend on the well-known pull-out effect mentioned in Ref 53; moreover, in the same investigation, a similar
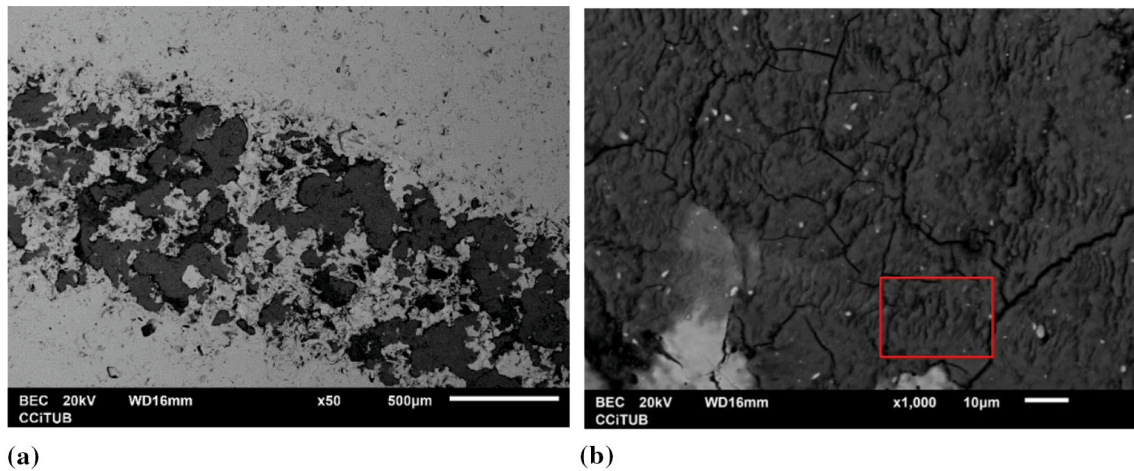
**Fig. 13** (a) Ball-on-disk wear track on APS coating, (b) high magnification, splat delamination (red box) (Color figure online)
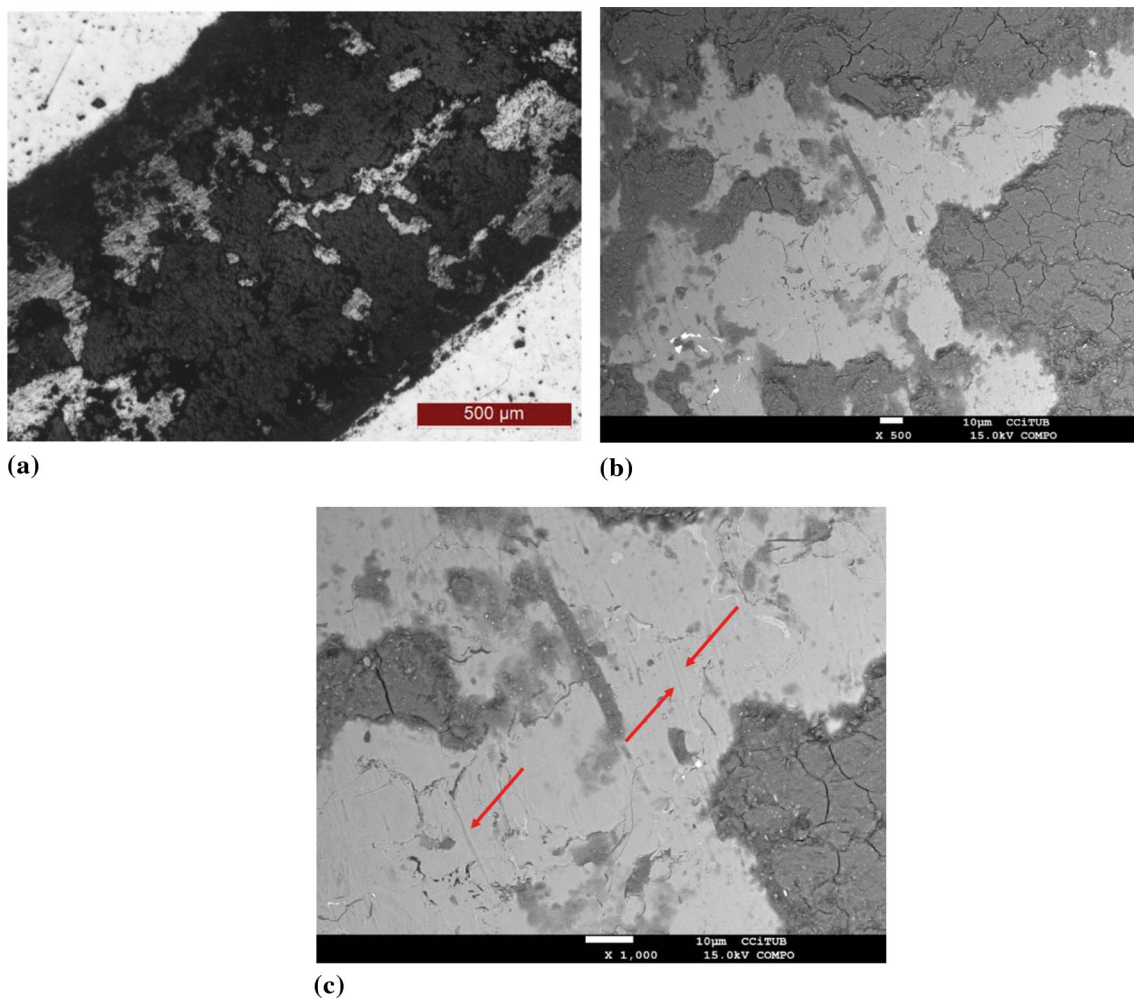


**Fig. 14** (a) Ball-on-disk wear track on HVOF coating, (b) high magnification, (c) wear grooves in the wear track

abrasive behavior was demonstrated for AlCoCrFeMo alloy deposited via flame spray process, due to the BCC microstructure of the coating. Abrasive resistance depends not only on microstructure, but also on the hardness (Ref 54) of the coating. Even if the hardness value of APS coating is greater than those of both 316L and C steel bulks

(Ref 22), the low oxides content of the coating did not ensure great wear resistance. The abrasive sand particles are bigger and harder than the deposited particles, and as a consequence of low oxides content and due to the high pressure at the contact point between abrasive particles and coating, the sand rip off the coating without resistance. Thereby, if the amount of hard phases in the APS coating is low, the hardness itself is not enough to protect the substrate. In contrast, the higher hardness of HVOF coating ensured better protection than APS one. At the beginning of the rubber wheel test, the abrasion rate of HVOF coating is lower than APS coating, and looking at Fig. 17, it is visible that after 1100 s also, the HVOF coating was completely abraded. Even if the thickness of the HVOF coating is less than half of APS coating (180 vs. 430 μm), the HVOF coating due to its hardness well-protects the substrate twice the time. During the rubber wheel test, sand abraded the coating but harder debris of HVOF coating did not remain in the wear track, as in the case of the ball-on-disk test. In addition, the rubber hardness is lower than the WC ball of ball-on-disk equipment, and for this reason, in Fig. 18, there are no deep grooves so, in comparison with

APS coating, it is possible to see a smoother surface with less amount of pores.

### Jet Erosion Test

As mentioned in ASTM G73-10, the results of an ideal jet erosion test would show the erosion slope divided into three regions, incubation region, acceleration region, and steady-state mass lost region. Some investigations on thermally sprayed coatings (Ref 55, 56, 57) did not observe the incubation stage due to the brittle of deposited coatings, and also in our investigation, the APS coating did not show this trend (Fig. 21). Figure 19 shows the morphology of the surface eroded by water droplets that appears smooth and plastically deformed, with craters, cracks, concavities, and overlaps.

The repeated impact against the water droplets caused severe plastic deformation of the coating, generating a high mass loss rate that cannot be compared with those of both 316L and C steel bulks, and once again, the hardness itself of the coating is not enough to resist the liquid impact. The presence of $Al_2O_3$ and the BCC microstructure of the APS
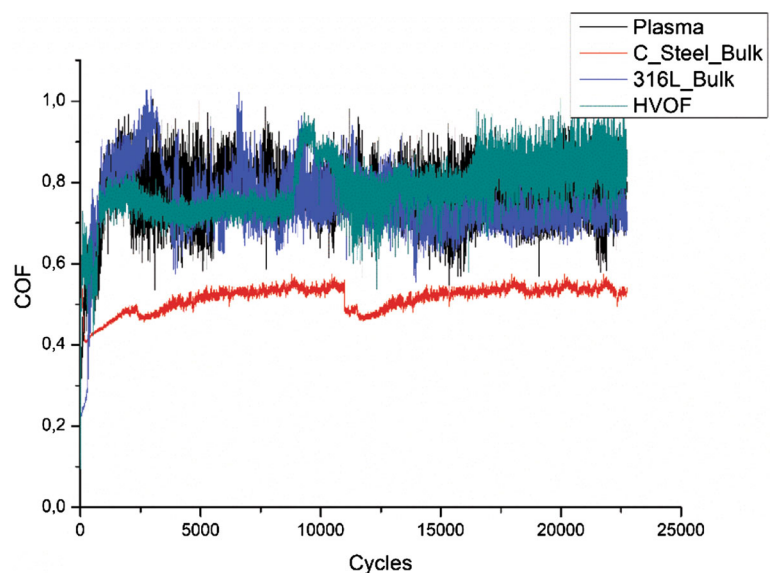
**Table 7** Ball-on-disk test results

|  | CoF | Wear rate ($mm^3$ $N^{-1}$ $m^{-1}$) |
|---|---|---|
| APS | $0.75 \pm 0.05$ | $5,75 \times 10^{-5}$ |
| 316L bulk | $0.65 \pm 0.08$ | $1.69 \times 10^{-4}$ |
| C steel bulk | $0.53 \pm 0.01$ | $3.06 \times 10^{-5}$ |
| HVOF | $0.78 \pm 0.07$ | $1,16 \times 10^{-4}$ |

**Table 8** Rubber wheel test results

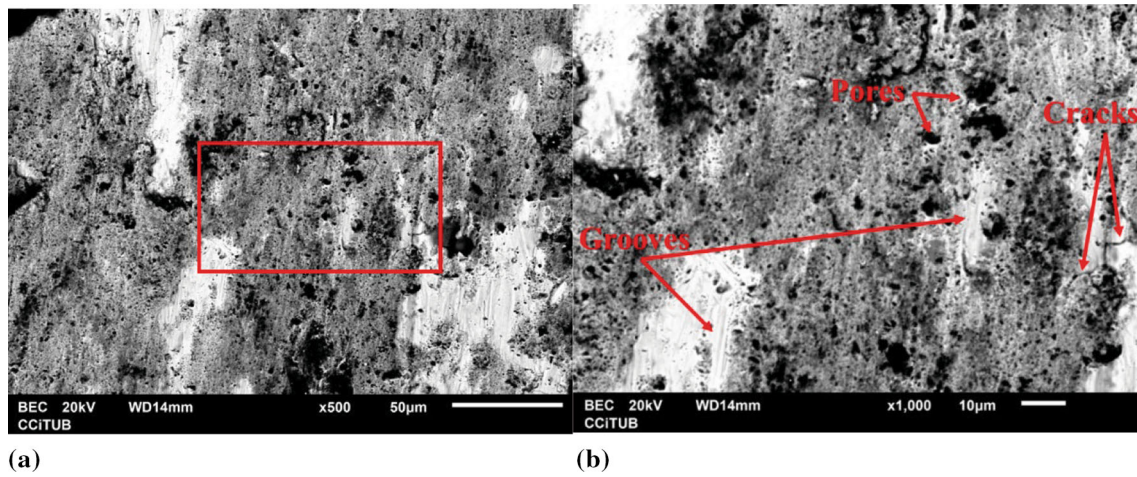|  | Abrasion rate ($mm^3$ $N^{-1}$ $m^{-1}$) |
|---|---|
| APS | $3.6 \times 10^{-4} \pm 1.54 \times 10^{-4}$ |
| 316L bulk | $2.0 \times 10^{-4} \pm 7.0 \times 10^{-5}$ |
| C steel bulk | $2.2 \times 10^{-4} \pm 6.5 \times 10^{-5}$ |
| HVOF | $2.5 \times 10^{-4} \pm 5.89 \times 10^{-5}$ |



**Fig. 15** CoF

**Fig. 16** (a) surface morphology after rubber wheel wear test on APS coating, (b) high magnification of red box area (Color figure online)
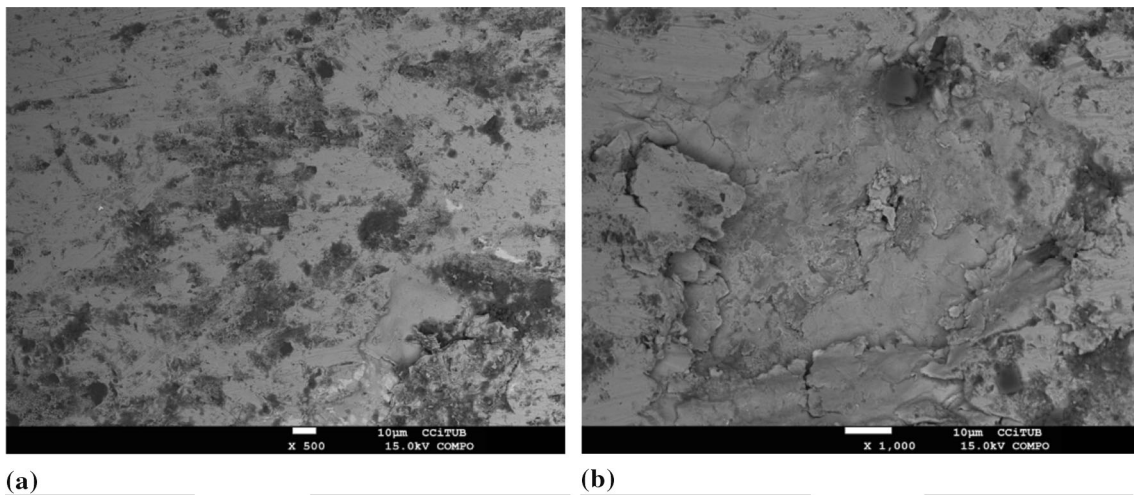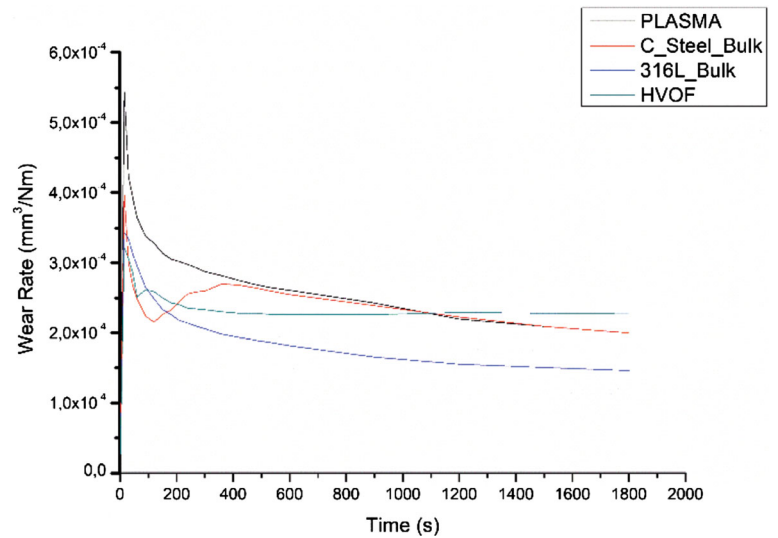
**Fig. 17** Rubber wheel





**Fig. 18** (a) surface morphology after rubber wheel wear test on HVOF coating, (b) high magnification
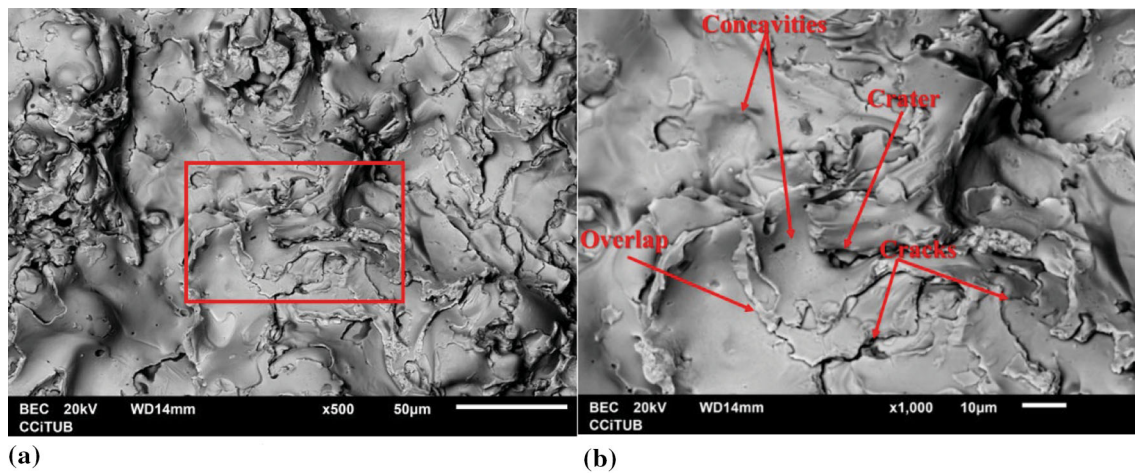
**Fig. 19** (a) surface morphology of jet erosion wear test on APS coating, (b) high magnification of red box area (Color figure online)
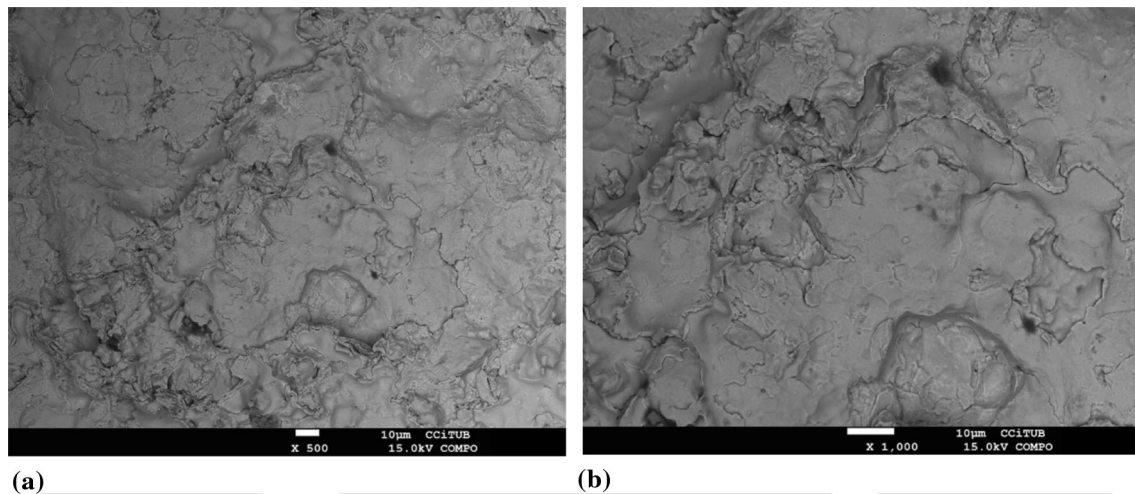


**Fig. 20** (a) surface morphology of jet erosion wear test on HVOF coating, (b) high magnification

coating seems not to be the best choice to resist erosion; in fact, the FCC alloys, such as Co-based alloys, are widely used in some industrial applications to preserve substrates against erosion (Ref 58). In our previous investigation (Ref 22), we have demonstrated that Cantor alloy coating deposited via HVOF protects the C steel substrate not only thanks to its FCC microstructure, but also due to the presence of Fe, Cr, and Mn oxides.

Figure 20 shows the damaged surface of the HVOF coating after the jet erosion test. As shown in Ref 59, the better performance of this coating in comparison with the APS one depends on its higher hardness and on the minor size of the craters and concavities on the eroded surface. Additionally, the HVOF coating surface seems to be smoother than the damaged APS surface, due to the less presence of overlaps. For this reason, the lateral outflow jets effect mentioned in Ref 60 has caused less damage during the test. The lateral outflow jets attack surfaces

characterized by more asperities and high roughness because, after the impact, the water droplets hit the irregularities of the surface and lift off the deposited particles, accelerating the growth of the cracks (Fig. 21).

## Conclusion

- AlCoCrFeNi HEAs starting feedstock powders were completely characterized in terms of shape, size, flow rate, apparent density, and microstructure;
- APS and HVOF techniques produced dense and thick coatings. The microstructural and mechanical properties of both coatings were analyzed, and their corrosion resistance and wear behavior were studied. In the case of the APS process, the coating thickness was $430 \pm 24$ μm, the hardness $HV_{0.3}$ was $367 \pm 22$, the porosity was $< 5\%$, and the adhesion strength was

**Fig. 21** Jet erosion test
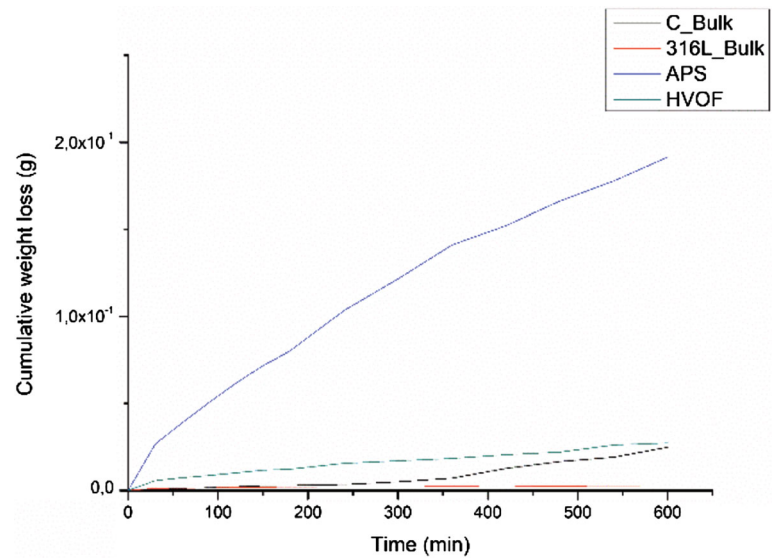


61 ± 3 MPa. The main phases present were BCC, with a low amount of oxides. The same BCC phases were detected by XRD analysis in HVOF coatings, and the thickness was 186 ± 10 μm, the hardness 502 ± 46 $HV_{0.3}$, the porosity < 2%, and the adhesion strength 15 ± 1 MPa. The poor adhesion strength of HVOF coating is probably due to the SOD distance, because OM and SEM images are visible particles not completely melted or not well-deformed;

- Both the APS and HVOF coatings well-protected the C steel substrate from corrosion in 3.5% NaCl, even if both are far from 316L performance, probably due to the low oxides content of the coatings;

- Ball on disk, rubber wheel, and jet erosion tests of APS coatings indicated a mass loss rate greater than those of both C steel and 316L substrates used to benchmark the performances. Even if the hardness of the coating is $HV_{0.3}$ 367 ± 22, the low amount of oxides did not act to improve wear resistance. HVOF coating ensures better performances in rubber wheel and jet erosion tests, but its performance in the ball-on-disk test is worse because of the debris remaining in the wear track, acting as a harder third body.

**Author Contributions** Conceptualization was done by AS and IGC; methodology was done by AS and IGC; validation was done by AS; formal analysis was done by AS, ETD, ERR, and IGC; investigation was done by AS, ETD, ERR, and IGC; resources were done by AS and IGC; data curation was done by AS, ETD, and ERR; writing—original draft preparation were done by AS; writing—review and editing were done by AS and IGC; supervision was done by IGC; project administration was done by AS and IGC; funding acquisition was done by AS and IGC.

# References

1. J.W. Yeh et al., Nanostructured high-Entropy Alloys with Multiple Principal Elements: Novel Alloy Design Concepts and Outcomes, *Adv. Eng. Mater.*, 2004, **6**(5), p 299-303. https://doi.org/10.1002/adem.200300567

2. B. Cantor, I.T.H. Chang, P. Knight, and A.J.B. Vincent, Microstructural Development in Equiatomic Multicomponent Alloys, *Mater. Sci. Eng. A*, 2004, **375-377**, p 213-218. https://doi.org/10.1016/j.msea.2003.10.257

3. F.Y. Shu et al., Structure and High-Temperature Property of Amorphous Composite Coating Synthesized by Laser Cladding FeCrCoNiSiB High-Entropy Alloy Powder, *J. Alloys Compd.*, 2018, **731**, p 662-666. https://doi.org/10.1016/j.jallcom.2017.08.248

4. G. Qin, W. Xue, R. Chen, H. Zheng, L. Wang, S. Yanqing, H. Ding, J. Guo, and F. Hengzhi, Grain Refinement and FCC Phase Formation in AlCoCrFeNi High Entropy Alloys by the Addition

of Carbon, *Materialia*, 2019, **6**, p 100259. https://doi.org/10.1016/j.mtla.2019.100259

5. P.L.J. Conway, T.P.C. Klaver, J. Steggo, and E. Ghassemali, High Entropy Alloys Towards Industrial Applications: High-Throughput Screening and Experimental Investigation, *Mater. Sci. Eng. A*, 2022, **830**, p 142297. https://doi.org/10.1016/j.msea.2021.142297

6. Y.F. Ye, Q. Wang, J. Lu, C.T. Liu, and Y. Yang, High-Entropy Alloy: Challenges and Prospects, *Mater. Today*, 2016, **19**(6), p 349-362. https://doi.org/10.1016/j.mattod.2015.11.026

7. Y. Zhang, T.T. Zuo, Z. Tang, M.C. Gao, K.A. Dahmen, P.K. Liaw, and L. Zhao Ping, Microstructures and Properties of High-Entropy Alloys, *Progr. Mater. Sci.*, 2014, **61**, p 1-93. https://doi.org/10.1016/j.pmatsci.2013.10.001

8. Y. Qiu, S. Thomas, M.A. Gibson, H.L. Fraser, and N. Birbilis, Corrosion of High Entropy Alloys, *Npj Mater. Degrad.*, 2017, **1**(1), p 1-17. https://doi.org/10.1038/s41529-017-0009-y

9. D. Wu, J.S.C. Jang, and T.G. Nieh, Elastic and Plastic Deformations in a High Entropy Alloy Investigated Using a Nanoindentation Method, *Intermetallics (Barking)*, 2016, **68**, p 118-127. https://doi.org/10.1016/j.intermet.2015.10.002

10. Y. Pan, J.-X. Liu, T.-Z. Tu, W. Wang, and G.-J. Zhang, High-Entropy Oxides for Catalysis: A Diamond in the Rough, *Chem. Eng. J.*, 2023, **451**, p 138659. https://doi.org/10.1016/j.cej.2022.138659

11. X.J. Fan, R.T. Qu, and Z.F. Zhang, Remarkably High Fracture Toughness of HfNbTaTiZr Refractory High-Entropy Alloy, *J. Mater. Sci .Technol.*, 2022, **123**, p 70-77. https://doi.org/10.1016/j.jmst.2022.01.017

12. S. Zeng, Y. Zhu, W. Li, H. Zhang, H. Zhang, and Z. Zhu, A Single-Phase $Ti_3Zr_{1.5}NbVAl_{0.25}$ Refractory high Entropy Alloy with Excellent Combination of Strength and Toughness, *Mater. Lett.*, 2022, **323**, p 132548. https://doi.org/10.1016/j.matlet.2022.132548

13. M. Fu, X. Ma, K. Zhao, X. Li, and D. Su, High-Entropy Materials for Energy-Related Applications, *Iscience*, 2021, **24**(3), p 102177.

14. A. Meghwal et al., Multiscale Mechanical Performance and Corrosion Behaviour of Plasma Sprayed AlCoCrFeNi High-Entropy Alloy Coatings, *J. Alloys Compd.*, 2021, **854**, p 157140. https://doi.org/10.1016/j.jallcom.2020.157140

15. F. Zhang, L. Wang, S. Yan, Y. Guangxing, J. Chen, and F. Yin, High Temperature Oxidation behavior of Atmosphere Plasma Sprayed AlCoCrFeNi High-Entropy Alloy Coatings, *Mater. Chem. Phys.*, 2022, **282**, p 125939. https://doi.org/10.1016/j.matchemphys.2022.125939

16. Y. Wang, S. Ma, X. Chen, J. Shi, Y. Zhang, and J. Qiao, Optimizing Mechanical Properties of AlCoCrFeNiTi$_x$ High-Entropy Alloys by Tailoring Microstructures, *Acta Metall. Sin. (English Letters)*, 2013, **26**(3), p 277-284. https://doi.org/10.1007/s40195-012-0174-5

17. K.B. Zhang et al., Microstructure and Mechanical Properties of CoCrFeNiTiAl$_x$ High-Entropy Alloys, *Mater. Sci. Eng. A*, 2009, **508**(1-2), p 214-219. https://doi.org/10.1016/j.msea.2008.12.053

18. L.H. Tian, W. Xiong, C. Liu, S. Lu, and M. Fu, Microstructure and Wear Behavior of Atmospheric Plasma-Sprayed AlCoCrFeNiTi High-Entropy Alloy Coating, *J. Mater. Eng. Perform.*, 2016, **25**(12), p 5513-5521. https://doi.org/10.1007/s11665-016-2396-6

19. A. Meghwal et al., Nano- and Micro-Mechanical Properties and Corrosion Performance of a HVOF Sprayed AlCoCrFeNi High-Entropy Alloy Coating, *J. Alloys Compd.*, 2022, **912**, p 165000. https://doi.org/10.1016/j.jallcom.2022.165000

20. M. Löbel, T. Lindner, T. Mehner, L.-M. Rymer, S. Björklund, S. Joshi, and T. Lampke, Microstructure and Corrosion Properties of AlCrFeCoNi High-Entropy Alloy Coatings Prepared by HVAF

and HVOF, *J. Thermal Spray Technol.*, 2022, **31**(1-2), p 247-255. https://doi.org/10.1007/s11666-021-01255-2

21. B. Preuß, T. Lindner, T. Uhlig, G. Wagner, and T. Lampke, Niobium and Molybdenum as Alloying Constituents in Al$_{0.3}$-CoCrFeNi to Develop Eutectic High-Entropy Alloys for HVOF Spraying, *J. Thermal Spray Technol.*, 2022 https://doi.org/10.1007/s11666-022-01417-w

22. A. Silvello, P. Cavaliere, S. Yin, R. Lupoi, I. Garcia Cano, and S. Dosta, Microstructural, Mechanical and Wear Behavior of HVOF and Cold-Sprayed High-Entropy Alloys (HEAs) Coatings, *J. Thermal Spray Technol.*, 2022, **31**(4), p 1184-1206. https://doi.org/10.1007/s11666-021-01293-w

23. S. Özbilen, Satellite Formation Mechanism in Gas Atomized Powders, *Powder Metall.*, 1999, **42**(1), p 70-78. https://doi.org/10.1179/pom.1999.42.1.70

24. L. Wang et al., Microstructure Evolution and Mechanical Properties of Atmosphere Plasma Sprayed AlCoCrFeNi High-Entropy Alloy Coatings under Post-Annealing, *J. Alloys Compd.*, 2021, **872**, p 159607. https://doi.org/10.1016/j.jallcom.2021.159607

25. Y. Ma et al., The BCC/B2 Morphologies in Al$_x$NiCoFeCr High-Entropy Alloys, *Metals*, 2017, **7**(2), p 57. https://doi.org/10.3390/met7020057

26. S. Dosta, M. Robotti, S. Garcia-Segura, E. Brillas, I.G. Cano, and J.M. Guilemany, Influence of Atmospheric Plasma Spraying on the Solar Photoelectro-Catalytic Properties of TiO$_2$ Coatings, *Appl. Catal. B*, 2016, **189**, p 151-159. https://doi.org/10.1016/j.apcatb.2016.02.048

27. J.M. Guilemany, N. Cinca, S. Dosta, and I.G. Cano, FeAl and NbAl$_3$ Intermetallic-HVOF Coatings: Structure and Properties, *J. Therm. Spray Technol.*, 2009, **18**(4), p 536-545. https://doi.org/10.1007/s11666-009-9339-9

28. A.G. Bulnes, V.A. Fuentes, I.G. Cano, and S. Dosta, Understanding the Influence of High Velocity Thermal Spray Techniques on the Properties of Different Anti-Wear WC-Based Coatings, *Coatings*, 2020, **10**(12), p 1-17. https://doi.org/10.3390/coatings10121157

29. B. Garrido, I.G. Cano, and S. Dosta, Adhesion Improvement and In Vitro Characterisation of 45S5 Bioactive Glass Coatings Obtained by Atmospheric Plasma Spraying, *Surf. Coat. Technol.*, 2021, **405**, p 126560. https://doi.org/10.1016/j.surfcoat.2020.126560

30. T. Li, Y. Liu, B. Liu, W. Guo, and X. Liyou, Microstructure and Wear Behavior of FeCoCrNiMo$_{0.2}$ High Entropy Coatings Prepared by Air Plasma Spray and the High Velocity Oxy-Fuel Spray Processes, *Coatings*, 2017, **7**(9), p 151. https://doi.org/10.3390/coatings7090151

31. S. Liu and W.G. Huang, Microstructure and Mechanical Performanceof AlCoCrNiSi$_x$ High-Entropy Alloys, *J. Mater. Eng.*, 2012, **1**, p 222-227.

32. J.K. Xiao, T.T. Li, Y.Q. Wu, J. Chen, and C. Zhang, Microstructure and Tribological Properties of Plasma-Sprayed CoCrFeNi-Based High-Entropy Alloy Coatings Under Dry and Oil-Lubricated Sliding Conditions, *J. Therm. Spray Technol.*, 2021, **30**(4), p 926-936. https://doi.org/10.1007/s11666-021-01175-1

33. J.-K. Xiao, W. Yu-Qing, J. Chen, and C. Zhang, Microstructure and Tribological Properties of Plasma Sprayed FeCoNiCrSiAl$_x$ High Entropy Alloy Coatings, *Wear*, 2020, **448-449**, p 203209. https://doi.org/10.1016/j.wear.2020.203209

34. P.J. Callus and C.C. Berndt, Relationships Between the Mode II Fracture Toughness and Microstructure of Thermal Spray Coatings, *Surf. Coat. Technol.*, 1999, **114**(2-3), p 114-128. https://doi.org/10.1016/S0257-8972(99)00018-3

35. P.F. Zhao, C.A. Sun, X.Y. Zhu, F.L. Shang, and C.J. Li, Fracture Toughness Measurements of Plasma-Sprayed Thermal Barrier Coatings Using a Modified Four-Point Bending Method, *Surf.*

*Coat. Technol.*, 2010, **204**(24), p 4066-4074. https://doi.org/10.1016/j.surfcoat.2010.05.029

36. Z. Tang, T. Yuan, C.W. Tsai, J.W. Yeh, C.D. Lundin, and P.K. Liaw, Fatigue Behavior of a Wrought Al$_{0.5}$CoCrCuFeNi Two-Phase High-Entropy Alloy, *Acta Mater.*, 2015, **99**, p 247-258. https://doi.org/10.1016/j.actamat.2015.07.004

37. M. Löbel, T. Lindner, S. Clauß, R. Pippig, D. Dietrich, and T. Lampke, Microstructure and Wear Behavior of the High-Velocity-Oxygen-Fuel Sprayed and Spark Plasma Sintered High-Entropy Alloy AlCrFeCoNi, *Adv. Eng. Mater.*, 2021, **23**(4), p 2001253. https://doi.org/10.1002/adem.202001253

38. E. Ghassemali, R. Sonkusare, K. Biswas, and N.P. Gurao, In-situ Study of Crack Initiation and Propagation in a Dual Phase AlCoCrFeNi High Entropy Alloy, *J. Alloys Compd.*, 2017, **710**, p 539-546. https://doi.org/10.1016/j.jallcom.2017.03.307

39. K.-C. Cheng, J.-H. Chen, S. Stadler, and S.-H. Chen, Properties of Atomized AlCoCrFeNi High-Entropy Alloy Powders and their Phase-Adjustable Coatings Prepared via Plasma Spray Process, *Appl. Surf. Sci.*, 2019, **478**, p 478-486. https://doi.org/10.1016/j.apsusc.2019.01.203

40. A. Valarezo, K. Shinoda, and S. Sampath, Effect of Deposition Rate and Deposition Temperature on Residual Stress of HVOF-Sprayed Coatings, *J. Therm. Spray Technol.*, 2020, **29**(6), p 1322-1338. https://doi.org/10.1007/s11666-020-01073-y

41. R. Trache, L.-M. Berger, and C. Leyens. Comparison of Alumina-Titania Coatings Deposited by Plasma and HVOF Spray Techniques. 2014.

42. A. Iqbal, S. Siddique, M. Maqsood, M.A.U. Rehman, and M. Yasir, Comparative Analysis on the Structure and Properties of Iron-Based Amorphous Coating Sprayed with the Thermal Spraying Techniques, *Coatings*, 2020, **10**(10), p 1006. https://doi.org/10.3390/coatings10101006

43. Y.C. Li, C. Zhang, W. Xing, S.F. Guo, and L. Liu, Design of Fe-Based Bulk Metallic Glasses with Improved Wear Resistance, *ACS Appl. Mater. Interfaces*, 2018, **10**(49), p 43144-43155. https://doi.org/10.1021/acsami.8b11561

44. W. Tillmann, C. Schaak, L. Hagen, G. Mauer, and G. Matthäus, Internal Diameter Coating Processes for Bond Coat (HVOF) and Thermal Barrier Coating (APS) Systems, *J. Therm. Spray Technol.*, 2019, **28**(1-2), p 233-241. https://doi.org/10.1007/s11666-018-0781-4

45. B. Sadeghi, P. Cavaliere, A. Perrone, and A. Silvello, Crack Initiation and Growth Behavior of HVOF Stellite-6 Coatings under Bending Loading, *Powders*, 2022, **1**(2), p 62-74. https://doi.org/10.3390/powders1020006

46. J.T. Liang, K.C. Cheng, and S.H. Chen, Effect of Heat Treatment on the Phase Evolution and Mechanical Properties of Atomized AlCoCrFeNi High-Entropy Alloy Powders, *J. Alloys Compd.*, 2019, **803**, p 484-490. https://doi.org/10.1016/j.jallcom.2019.06.301

47. W. Li, D. Xie, D. Li, Y. Zhang, Y. Gao, and P.K. Liaw, Mechanical Behavior of High-Entropy Alloys, *Progr. Mater. Sci.*, 2021, **118**, p 100777. https://doi.org/10.1016/j.pmatsci.2021.100777

48. N. W. Satya, S. Mudiantoro, and W. Winarto, Bond Strength, Hardness, and Microstructure Analysis of Stellite Coating Applied on 410 Steel Surface Using Flame Spray, Plasma Spray, and High-Velocity Oxyfuel Spray Process, *IOP Conf. Ser. Mater. Sci. Eng.*, 2020, **924**(1), p 012016. https://doi.org/10.1088/1757-899X/924/1/012016

49. K. Palanisamy, S. Gangolu, and J. M. Antony, Effects of HVOF Spray Parameters on Porosity and Hardness of 316L SS Coated Mg AZ80 Alloy, *Surf. Coat. Technol.*, 2022, **448**, p 128898. https://doi.org/10.1016/j.surfcoat.2022.128898

50. M. Xue, X. Mao, Y. Lv, Y. Chi, Y. Yang, J. He, and Y. Dong, Comparison of Micro-Nano FeCoNiCrAl and FeCoNiCrMn Coatings Prepared from Mechanical Alloyed High-Entropy Alloy Powders, *J. Thermal Spray Technol.*, 2021, **30**(6), p 1666-1678. https://doi.org/10.1007/s11666-021-01210-1

51. A. Ohmori and C.-J. Li, Quantitative Characterization of the Structure of Plasma-Sprayed Al$_2$O$_3$ Coating by Using Copper Electroplating, *Thin Solid Films*, 1991, **201**(2), p 241-252. https://doi.org/10.1016/0040-6090(91)90114-D

52. S. Mahade, A. Mulone, S. Björklund, U. Klement, and S. Joshi, Investigating Load-Dependent Wear Behavior and Degradation Mechanisms in Cr$_3$C$_2$-NiCr Coatings Deposited by HVAF and HVOF, *J. Market. Res.*, 2021, **15**, p 4595-4609. https://doi.org/10.1016/j.jmrt.2021.10.088

53. R.B. Nair, G. Perumal, and A. McDonald, Effect of Microstructure on Wear and Corrosion Performance of Thermally Sprayed AlCoCrFeMo High-Entropy Alloy Coatings, *Adv. Eng. Mater.*, 2022 https://doi.org/10.1002/adem.202101713

54. N.M. Melendez, V.V. Narulkar, G.A. Fisher, and A.G. McDonald, Effect of Reinforcing Particles on the Wear Rate of Low-Pressure Cold-Sprayed WC-Based MMC Coatings, *Wear*, 2013, **306**(1-2), p 185-195. https://doi.org/10.1016/j.wear.2013.08.006

55. H. Assadi et al., On Parameter Selection in Cold Spraying, *J. Therm. Spray Technol.*, 2011, **20**(6), p 1161-1176. https://doi.org/10.1007/s11666-011-9662-9

56. J.M. Guilemany, M. Torrell, and J.R. Miguel, Study of the HVOF Ni-Based Coatings' Corrosion Resistance Applied on Municipal Solid-Waste Incinerators, *J. Thermal Spray Technol.*, 2008, **17**(2), p 254-262. https://doi.org/10.1007/s11666-008-9167-3

57. M. Torrell, S. Dosta, J.R. Miguel, and J.M. Guilemany, Optimisation of HVOF Thermal Spray Coatings for their Implementation as MSWI Superheater Protectors, *Corros. Eng. Sci. Technol.*, 2010, **45**(1), p 84-93. https://doi.org/10.1179/147842209X12601838533508

58. B. Liu and Y. Chen, Effects of Cobalt Content on the Microstructure, Mechanical Properties and Cavitation Erosion Resistance of HVOF Sprayed Coatings, *Coatings*, 2019, **9**(9), p 534. https://doi.org/10.3390/coatings9090534

59. A.K. Gujba, M.S. Mahdipoor, and M. Medraj, Water Droplet Impingement Erosion Performance of WC-Based Coating Sprayed by HVAF and HVOF, *Wear*, 2021, **484-485**, p 203904. https://doi.org/10.1016/j.wear.2021.203904

60. M.S. Mahdipoor, F. Tarasi, C. Moreau, A. Dolatabadi, and M. Medraj, HVOF Sprayed Coatings of Nano-Agglomerated Tungsten-Carbide/Cobalt Powders for Water Droplet Erosion Application, *Wear*, 2015, **330-331**, p 338-347. https://doi.org/10.1016/j.wear.2015.02.034